



Article

# Mixed-Phase $\text{Fe}_2\text{O}_3$ Derived from Natural Hematite Ores/ $\text{C}_3\text{N}_4$ Z-Scheme Photocatalyst for Ofloxacin Removal

Sulakshana Shenoy <sup>1</sup>, Mohsen M. Farahat <sup>1,2</sup>, Chitiphon Chuaicham <sup>1</sup>, Karthikeyan Sekar <sup>1,3</sup>, Boopathy Ramasamy <sup>4</sup> and Keiko Sasaki <sup>1,\*</sup>

<sup>1</sup> Department of Earth Resources Engineering, Faculty of Engineering, Kyushu University, 744 Motooka, Nishiku, Fukuoka 819-0395, Japan; sulakshana@mine.kyushu-u.ac.jp (S.S.); mohsen105@hotmail.com (M.M.F.); song@mine.kyushu-u.ac.jp (C.C.); karthiks1@srmist.edu.in (K.S.)

<sup>2</sup> Central Metallurgical Research and Development Institute (CMRDI), P.O. Box 87, Helwan, Cairo 11421, Egypt

<sup>3</sup> Department of Chemistry, Faculty of Engineering and Technology, SRM Institute of Science and Technology, Kattankulathur 603203, Tamil Nadu, India

<sup>4</sup> Environment & Sustainability Department, Institute of Minerals and Materials Technology (CSIR-IMMT), Bhubaneswar 751013, Odisha, India; chemboopathy@gmail.com

\* Correspondence: keikos@mine.kyushu-u.ac.jp; Tel./Fax: +81-92-802-3338

**Abstract:** Abatement of pharmaceutical pollutants from aquatic systems is crucial but remains a challenge. Semiconductor photocatalysis has emerged as an eco-friendly technique that utilizes renewable solar energy to address environmental issues. Naturally occurring and earth abundant hematite ( $\text{Fe}_2\text{O}_3$ ) ores can be incorporated as a suitable component of a photocatalyst. Herein, Brazilian hematite was partially phase transformed into heterophase (consisting of  $\alpha/\gamma\text{-Fe}_2\text{O}_3$ ) by a simple single-stage heat treatment procedure. The method of synthesis was simple and economical, requiring neither solvents nor concentrated acids. The existence of  $\alpha/\gamma$ -phases in the produced  $\text{Fe}_2\text{O}_3$  (FO) was confirmed by X-ray diffraction analysis. After the phase transformation process, the local structure surrounding the Fe atoms was varied as evidenced from X-ray absorption spectroscopy. Given its low toxicity, narrow bandgap, and chemical stability, FO was further combined with g- $\text{C}_3\text{N}_4$  (CN) to form composites. The optical properties of the synthesized CNFO composites confirmed that the visible light harvesting ability of CN was enhanced after combining with FO. The CN sheets were grown uniformly over the surface of FO as evidenced from scanning electron microscopy. The prepared composites could degrade an aqueous solution of ofloxacin (OFX, 10 ppm) under visible light with remarkable efficacy. The performance of CNFO-5% was 4.8 times higher when compared to pure CN. The initial rate constant value for the photocatalytic degradation of OFX by CNFO-5% was  $0.1271 \text{ min}^{-1}$ . The catalyst was stable even after five repeated cycles of photodegradation. The photoluminescence spectra and electrochemical measurements confirmed the efficient separation and transfer of the photogenerated charges across their interface. The investigations on different scavengers demonstrated that superoxide anion radicals and holes played a significant role in the degradation of OFX. The mechanism for the charge transfer was proposed to be a Z-scheme heterojunction. These results point to the potential of using inexpensive, abundant, and recyclable natural hematite ores as state-of-the-art photocatalysts for the elimination of pharmaceuticals in wastewater.



**Citation:** Shenoy, S.; Farahat, M.M.; Chuaicham, C.; Sekar, K.; Ramasamy, B.; Sasaki, K. Mixed-Phase  $\text{Fe}_2\text{O}_3$  Derived from Natural Hematite Ores/ $\text{C}_3\text{N}_4$  Z-Scheme Photocatalyst for Ofloxacin Removal. *Catalysts* **2023**, *13*, 792. <https://doi.org/10.3390/catal13050792>

Academic Editor: Xu Xiang

Received: 3 April 2023

Revised: 18 April 2023

Accepted: 21 April 2023

Published: 23 April 2023

**Keywords:** graphitic carbon nitride; hematite mineral ore; photodegradation; ofloxacin



**Copyright:** © 2023 by the authors. Licensee MDPI, Basel, Switzerland. This article is an open access article distributed under the terms and conditions of the Creative Commons Attribution (CC BY) license (<https://creativecommons.org/licenses/by/4.0/>).

## 1. Introduction

Antibiotics, which are extensively used in human healthcare, veterinary, and aquaculture, are widely recognized as a serious pollutant [1]. These pharmaceuticals can enter waterways directly from manufacturing plants or through human and animal waste. A global study monitoring 1052 sampling sites along 258 rivers in 104 countries found that the presence of pharmaceutical contaminants in surface water poses a threat to environmental and/or human health in more than a quarter of the studied locations globally [2,3]. These

Toxins are notoriously hard to remove with regular wastewater treatment methods because they are resistant to biodegradation. Therefore, they are extremely dangerous to aquatic life and human health even at trace amounts. For instance, ofloxacin (OFX) is an antibiotic that belongs to the fluoroquinolone class. The human body does not fully metabolize fluoroquinolones. The amount of pharmacologically active fluoroquinolones excreted by the body ranges from 20% to 80% of the total amount consumed. Because of this, fluoroquinolones have an impact on household sewage systems [4]. Fluoroquinolones and other antimicrobials found in wastewater often remain in the water after treatment, which can be detrimental to aquatic and human life. Microorganisms exposed to antimicrobial residues in environmental matrices may have gene changes that make them resistant to the substance. Due to the rise of drug-resistant microorganisms, stronger medications are being utilized to treat diseases [5]. Therefore, it is critical that we establish a reliable strategy for effectively mineralizing these pollutants [6]. In comparison to the most common methods, the advanced oxidation processes seem to hold the most promise because of their capacity for the total degradation of these pollutants [7]. Fortunately, photocatalysis is emerging as a promising solution to overcome this issue. Photocatalysis is a process that involves the use of a photocatalyst, typically a semiconductor material, to break down pollutants in water when exposed to light. When light strikes the photocatalyst, it generates electron-hole pairs that react with water molecules to produce highly reactive radicals that can degrade organic contaminants. Studies have shown that photocatalysis can effectively remove various pharmaceutical compounds from wastewater, including antibiotics, analgesics, and hormones. Furthermore, the process is environmentally friendly, as it does not produce any harmful byproducts. However, there are still some challenges that need to be addressed to make photocatalysis a widely adopted technology for pharmaceutical wastewater treatment. These include the optimization of photocatalytic materials and reactor design, as well as the development of cost-effective and scalable processes [8–10].

Graphitic carbon nitride ( $\text{g-C}_3\text{N}_4$ ) has been intensively studied in photocatalysis due to its simple synthesis, extremely good visible-light harvesting capacity, environmental friendliness, and superior thermal/chemical stability [11,12]. This material has a layered structure with a bandgap that can be tuned by varying the degree of polymerization, making it suitable for photocatalytic applications. Studies have shown that  $\text{g-C}_3\text{N}_4$  can effectively decompose pharmaceutical pollutants under visible light irradiation, making it a potential solution for wastewater treatment [13]. However,  $\text{g-C}_3\text{N}_4$  has some drawbacks that limit its photocatalytic efficiency. The poor surface area, low separation efficiency, and rapid charge recombination severely restrict its photocatalytic efficacy [13]. For instance, a heterojunction between two different types of semiconductors, can be used to improve the efficiency and selectivity of photocatalysts. Some of the key requirements for the design of a heterojunction photocatalyst include spatial separation of photogenerated electron-hole pairs and the ability to absorb light across a broad wavelength range [14]. The coupling of carbon nitride with suitable semiconductors to construct composite photocatalysts is one of the most promising solutions proposed to facilitate the separation of charge carriers [15,16]. Due to synergistic effects between  $\text{g-C}_3\text{N}_4$  and the other suitable semiconductor, the  $\text{g-C}_3\text{N}_4$ -based heterostructures can also confer some novel properties on photocatalysts, as the heterostructures are composed of more than one component. It is possible that the rational design of heterostructures based on  $\text{g-C}_3\text{N}_4$  could provide potential approaches to produce highly efficient visible-light-driven photocatalysts for use in environmental remediation [17–20].

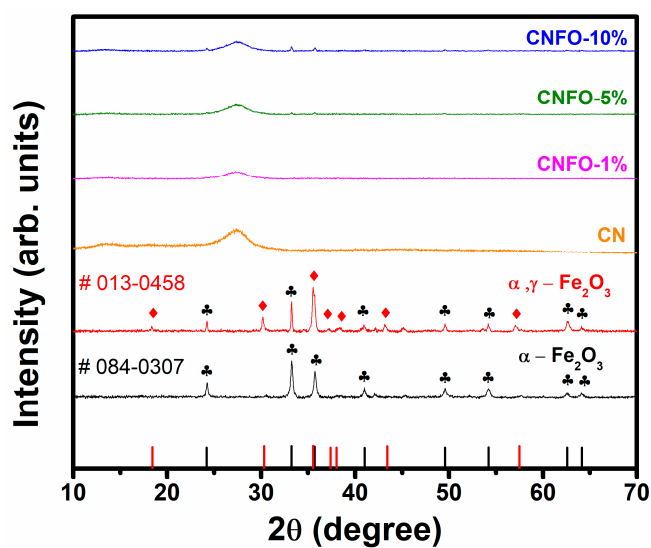
Metal oxide-based semiconductors are promising candidates for photocatalytic applications due to their good light absorption properties, charge-transfer characteristics, and excellent electronic structures. In recent years, the use of photocatalysts that are based on metal oxides has become increasingly common as a result of the potential applications that these catalysts offer in the field of wastewater treatment [21]. One material that has received significant attention as a photocatalyst is  $\text{Fe}_2\text{O}_3$ , also known as iron oxide or hematite [22,23]. In the crust of the Earth, the mineral hematite ( $\text{Fe}_2\text{O}_3$ ) is the most common

and stable iron oxide. It has remarkable corrosion resistance, high electrical conductivity, and a narrow bandgap of 1.9–2.2 eV [24,25].  $\text{Fe}_2\text{O}_3$  has also been shown to be effective in degrading pollutants in wastewater. In these reactions,  $\text{Fe}_2\text{O}_3$  absorbs light and produces reactive oxygen species that can break down organic pollutants into simpler, less harmful products. However, a low electron transport rate, a short hole migration range of approximately 2–4 nm, and fast recombination of charges result in weak performance [26]. One strategy to overcome constraints of  $\alpha\text{-Fe}_2\text{O}_3$  is to combine two different phases of  $\text{Fe}_2\text{O}_3$  to form a heterophase material [27]. Maghemite ( $\gamma\text{-Fe}_2\text{O}_3$ ) has a very similar structure to  $\alpha\text{-Fe}_2\text{O}_3$ , and its magnetic property makes it easy to collect the photocatalyst from the photocatalytic system [28]. For instance, Ghasemifard et al. synthesized  $\alpha/\gamma\text{-Fe}_2\text{O}_3$  nanoparticles following an auto-combustion technique [29]. A similar solution-combustion approach was utilized to prepare the mixed-phase  $\text{Fe}_2\text{O}_3$  particles [30]. To produce the final heterophase  $\text{Fe}_2\text{O}_3$  particles, however, such methods are not only prohibitively expensive but also reliant on a diverse range of metal precursors as well as highly concentrated acids. So, it is better to make use of the naturally occurring hematite ores that are easily accessible and transform them into the heterophase without resorting to any complex treatment procedures. In the current work, researchers claim to successfully convert hematite mineral ore to its heterophase form without the need of any solvents or concentrated acids, making the method both easy and cost-effective.

The naturally occurring hematite ore from Brazil was subjected to a simple and economically viable heat treatment technique in this study, which resulted in a partial phase transformation into mixed-phase  $\alpha/\gamma\text{-Fe}_2\text{O}_3$ . The ease of usage, absence of potentially harmful solvents, high efficiency, and absence of post-purification prerequisites are the primary advantages offered by this method of synthesis. In order to produce composites, the resulting mixed-phase  $\text{Fe}_2\text{O}_3$  was *in situ* combined with g-C<sub>3</sub>N<sub>4</sub> nanosheets [31]. The structural characterization confirmed that  $\text{Fe}_2\text{O}_3$  underwent a phase transition. In addition to this, as demonstrated by X-ray absorption spectroscopy, this caused a change in the local structure that was found in the vicinity of the iron atoms. The morphology of composites provided conclusive evidence that the presence of  $\text{Fe}_2\text{O}_3$  particles led to the uniform distribution of CN nanosheets over their surface. After the addition of mixed-phase  $\text{Fe}_2\text{O}_3$ , the ability of CN to absorb visible light was significantly enhanced. The photocatalytic performance of the synthesized photocatalysts were evaluated toward the degradation of ofloxacin under visible light irradiation. Based on scavenger studies, it was confirmed that superoxide anion radicals and holes were the main active species involved in the degradation reaction. Photoluminescence spectra and electrochemical measurements confirmed the effective separation of the photogenerated charge carriers. Depending on the band edge positions, a Z-scheme charge-transfer pathway was proposed.

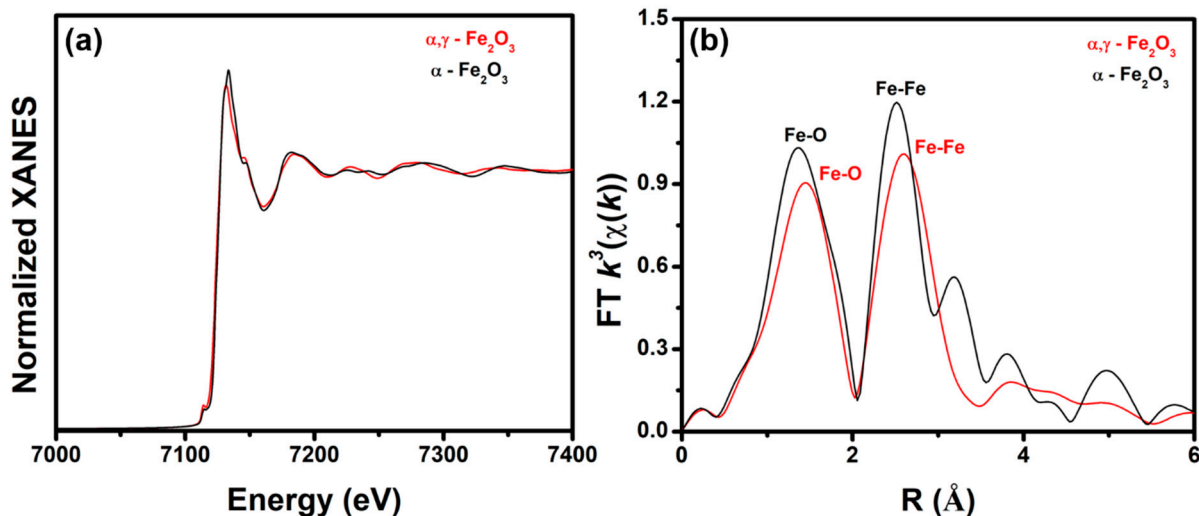
## 2. Results and Discussion

Figure 1 shows that CN has two characteristic diffraction peaks at 13.2° and 27.4°, which can be assigned to (1 0 0) and (0 0 2) planes of g-C<sub>3</sub>N<sub>4</sub>. The graphitic structure with aromatic ring stacking between layers is represented by the (0 0 2) peak, while the (1 0 0) peak is associated with an in-plane structural packing motif of tri-s-triazine units [32]. Pure hematite ore exhibits a  $\alpha\text{-Fe}_2\text{O}_3$  phase (represented by symbol ♣), which is correlating with JCPDS #084-0307. The prominent peaks are located and indexed at 24.20°, 33.23°, 35.70°, 40.95°, 49.57°, 54.20°, 62.58°, and 64.15°. After the partial phase transformation of  $\alpha\text{-Fe}_2\text{O}_3$  at 400 °C in the presence of polyethylene glycol, it shows additional peaks of  $\gamma\text{-Fe}_2\text{O}_3$  (represented by symbol ♦) as evident from the XRD plot. The major peak of  $\alpha\text{-Fe}_2\text{O}_3$  at 33.23° drops in intensity, and additional peaks corresponding to  $\gamma\text{-Fe}_2\text{O}_3$  arise at 18.43°, 30.33°, 35.74°, 37.37°, 37.99°, 43.42°, and 57.48°, respectively [33]. The  $\gamma\text{-Fe}_2\text{O}_3$  is a good index and match for JCPDS #013-0458. The resulting sample, therefore, consists of mixed-phase  $\alpha/\gamma\text{-Fe}_2\text{O}_3$ . There was no secondary phase transformation when the composite was formed between CN and different (1, 5, and 10 wt%) of FO. This confirms the stability and purity of the as-synthesized samples.



**Figure 1.** XRD patterns of  $\text{Fe}_2\text{O}_3$ , mixed-phase  $\text{Fe}_2\text{O}_3$ , and the CNFO composites.

In XANES spectra of the mixed-phase  $\text{Fe}_2\text{O}_3$ , the oscillation of the white line changed suggesting that local structure surrounding the Fe center atom is varied after the heat treatment process (Figure 2a). In Figure 2b, R space of EXAFS spectra of both  $\alpha$ - $\text{Fe}_2\text{O}_3$  and mixed-phase  $\text{Fe}_2\text{O}_3$  show two clear loops which are from Fe-O in the first shell and Fe-Fe in the second shell. Based on model structures of  $\alpha$ - $\text{Fe}_2\text{O}_3$  and  $\gamma$ - $\text{Fe}_2\text{O}_3$ , the first shell of both phases had six oxygen atoms surrounded by Fe center atoms. While the second shell of  $\alpha$ - $\text{Fe}_2\text{O}_3$  had seven Fe atoms with an average atomic distance of 3.07 Å. However, after the phase transformation process, the mixed-phase  $\text{Fe}_2\text{O}_3$  had twelve Fe atoms with an atomic distance of 3.18 Å higher than that of  $\alpha$ - $\text{Fe}_2\text{O}_3$  resulting in the shift of its second shell to a higher radial distance. This result can support the formation of the mixed-phase  $\text{Fe}_2\text{O}_3$ .



**Figure 2.** (a) Fe K-edge XANES and (b) the EXAFS spectrum for  $\alpha$ - $\text{Fe}_2\text{O}_3$  and mixed-phase  $\text{Fe}_2\text{O}_3$  as a Fourier transform ( $\text{FT } k^3\chi(k)$ ) function.

As can be seen in Figure 3a, micrometer-sized particles with an irregular shape are present in pristine  $\alpha$ - $\text{Fe}_2\text{O}_3$ . Even after being subjected to heat treatment, the mixed-phase  $\text{Fe}_2\text{O}_3$  did not exhibit a morphology that was considerably distinct from that of the parent ore (Figure 3b). Figure 3c shows that the pristine CN that was synthesized from the urea precursor had a morphology that resembled a porous sheet. When it comes to the adsorption of the catalyst on their surface, this porous structure offers several significant

benefits. The CN nanosheets were grown on the surface of the FO once the composite had been formed (Figure 3d). The efficient transfer of charge across the interface between the CN sheets, and the FO during the photocatalytic reaction is due to the strong adhesion of the CN sheets to the surface of the FO. As shown in Figure 3f–i, an EDX examination of the CNFO-5% composite demonstrates an even distribution of C and N over the surface of FO particles, hence verifying the considerable CN–FO interaction.

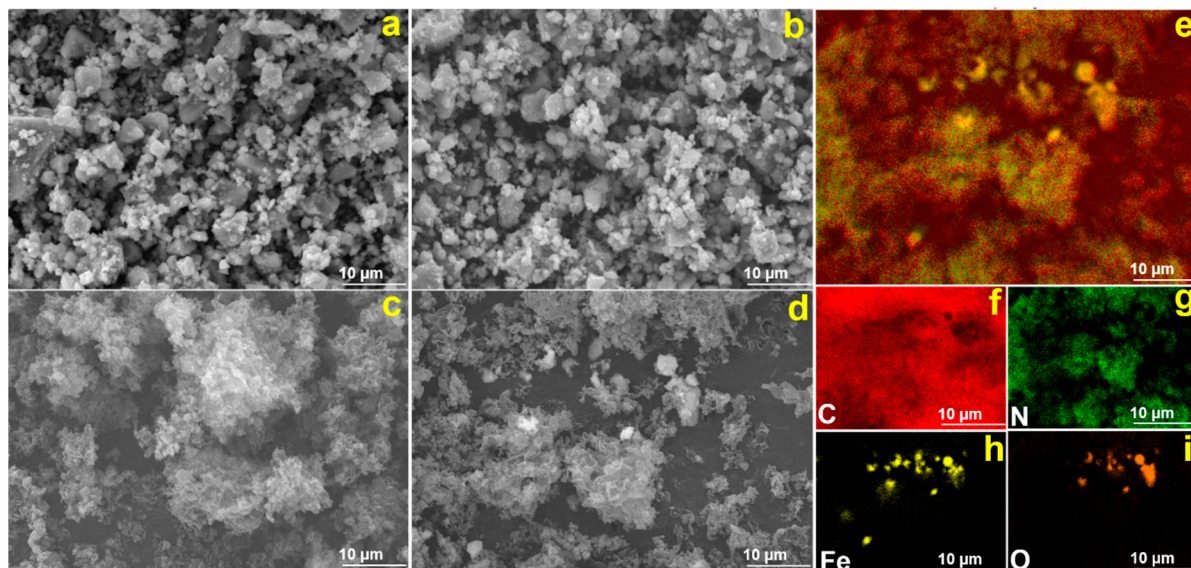


**Figure 3.** (a,b) Unevenly dispersed particles of  $\text{Fe}_2\text{O}_3$ , (c) porous sheets of CN, (d) growth of CN sheets over  $\text{Fe}_2\text{O}_3$  surface, and (e–i) corresponding EDX mapping of the region shown in (d).

Pristine CN shows an absorption at 464 nm, consistent with the reported literature [34]. As shown in Figure S1,  $\alpha$ - $\text{Fe}_2\text{O}_3$  and mixed-phase  $\text{Fe}_2\text{O}_3$  displayed absorption edges at 740 and 738 nm, respectively, with bandgap values of 1.67 and 1.68 eV. Following the addition of FO, the composite exhibited a change in its absorption edges toward longer wavelengths, as illustrated in Figure 4a. This change takes place as a result of the potent capacity of FO to absorb visible light, which boosts the effectiveness of the light harvesting ability and generates an increased number of charge carriers. In Figure 4b, bandgap ( $E_g$ ) values were calculated following the previously reported literature [35] and are found to be 2.49, 2.48, and 2.46 eV for CNFO-1%, CNFO-5%, and CNFO-10%, respectively.

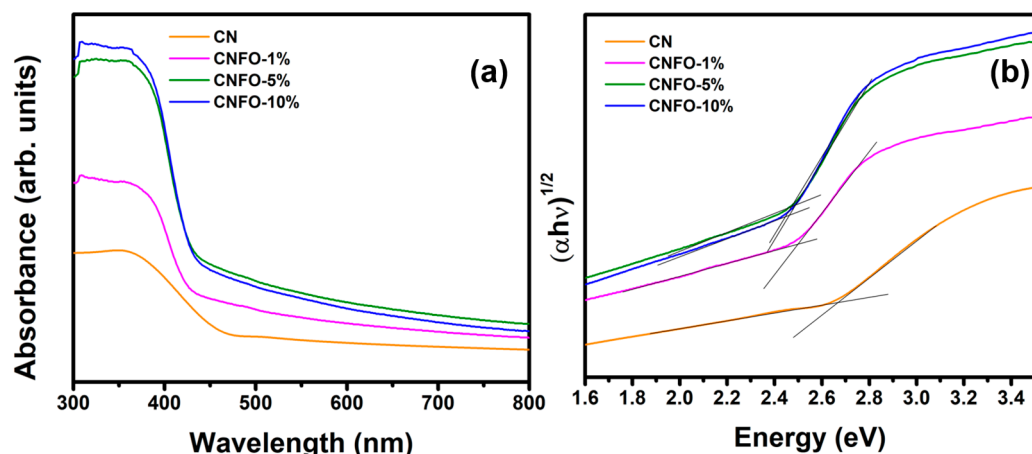


**Figure 4.** (a,b) UV-visible light absorption spectra and respective bandgap energies of synthesized photocatalysts.

Figure 5a presents the results of the surface area study performed on the CN, FO, and CNFO composites. CN nanosheets in their purest form have a surface area of  $37 \text{ m}^2 \text{ g}^{-1}$ , while FO only has a surface area of  $10 \text{ m}^2 \text{ g}^{-1}$ . The CNFO composite surface area increased as the FO concentration increased, and it was found to be  $43, 50$ , and  $57 \text{ m}^2 \text{ g}^{-1}$  for CNFO-1%, CNFO-5%, and CNFO-10%, respectively. The increased surface area that results from the formation of the composite between CN and FO may be favorable for the application of photocatalysis since it may render more surface for the adsorption of the pollutant.

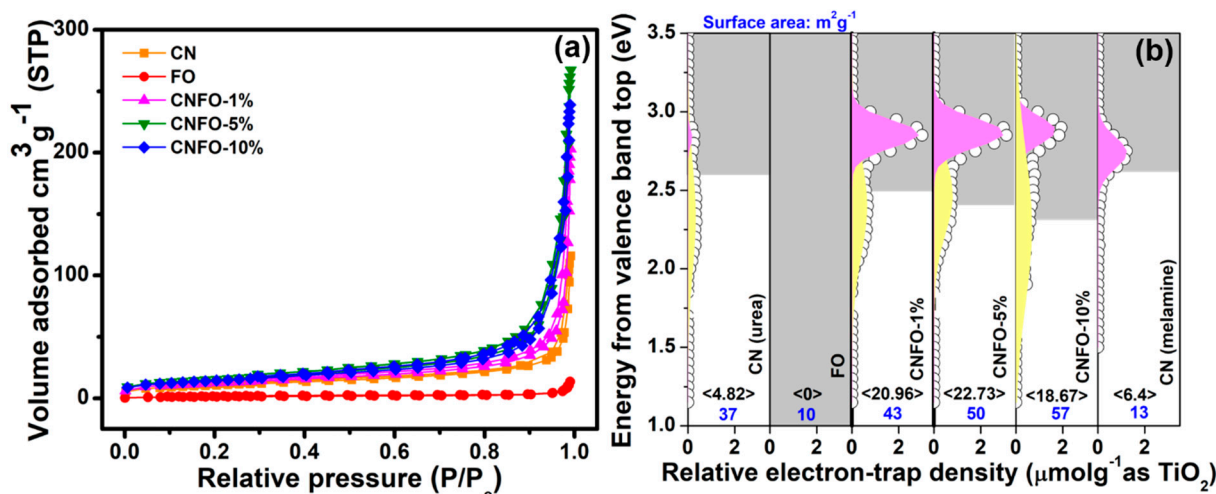


**Figure 5.** (a)  $\text{N}_2$  adsorption–desorption isotherms; (b) ERDT patterns and conduction band bottom (grey bars) for the as-synthesized photocatalysts.

Moreover, RDB-PAS was utilized to explore the surface electrical properties of the photocatalyst, including the distribution of electron trap states [36]. The electron density in the electron trap states of the generated CN from the urea precursor was low, and the peak of its electron accumulation density occurred somewhere between 2.0 and 3.0 eV, which is rather close to the bottom of the conduction band. After the formation of the composite, the trap states dramatically increased, and new trap states appeared in the region between 2.0 and 2.9 eV. This suggests that the introduction of FO generates some surface defect in CN, which results in the generation of new electron trap states on the surface of CN. This is demonstrated in Figure 5b. In addition, the peak position of the new trap state around 2.9 eV showed a higher position than a normal CN sheet-like structure (synthesized from melamine) around 2.7 eV. This indicates that the obtained porous CN sheet has a higher surface distortion in comparison to the normal CN sheet-like structure. Melamine was used in the synthesis of the material. Additionally, the surface of the FO acted as a foundational material for the development of CN sheets, which stopped the CN from aggregating on top of one another. The findings are in line with what was expected from the surface area analysis. In addition, the growth of new electron trap states with energies between 2.0 and 2.9 eV will be useful since these states can trap photoinduced charges and stop the recombination of charges.

The survey spectrum of XPS is displayed in Figure S2a. Figure 6a shows the sp<sup>2</sup> hybridization of the C-C bond related to the signal at 284.6 eV. The C-N-C group in CN was observed to have a binding energy (B.E.) of 285.4 eV. In addition, the signal at 287.2 eV could be the sp<sup>2</sup>-hybridized carbon in the N=C=N rings of the triazine compounds. Figure 6b shows that the three peaks of N 1 s at 397.7, 398.8, and 400.1 eV correspond to typical peaks of sp<sup>2</sup>-hybridized N atoms in C=N-C, N-(C)<sub>3</sub>, and -NH<sub>2</sub>, respectively. Two peaks can be seen in the high-resolution spectrum of Fe 2p. These peaks are located at 711.1 and 724.7 eV and can be attributed to Fe 2p<sub>3/2</sub> and Fe 2p<sub>1/2</sub>, respectively [32,37]. However, Fe 2p peaks in the CNFO-5% composite were of relatively low strength. Due to the in-situ

growth of CN nanosheets on the surface of  $\text{Fe}_2\text{O}_3$  and the minimal  $\text{Fe}_2\text{O}_3$  content of the composite, the entire surface of the FO was covered by CN sheets. Hence, little Fe content was exposed on the surface of composite, making it challenging to obtain Fe 2p signals in the XPS analysis.

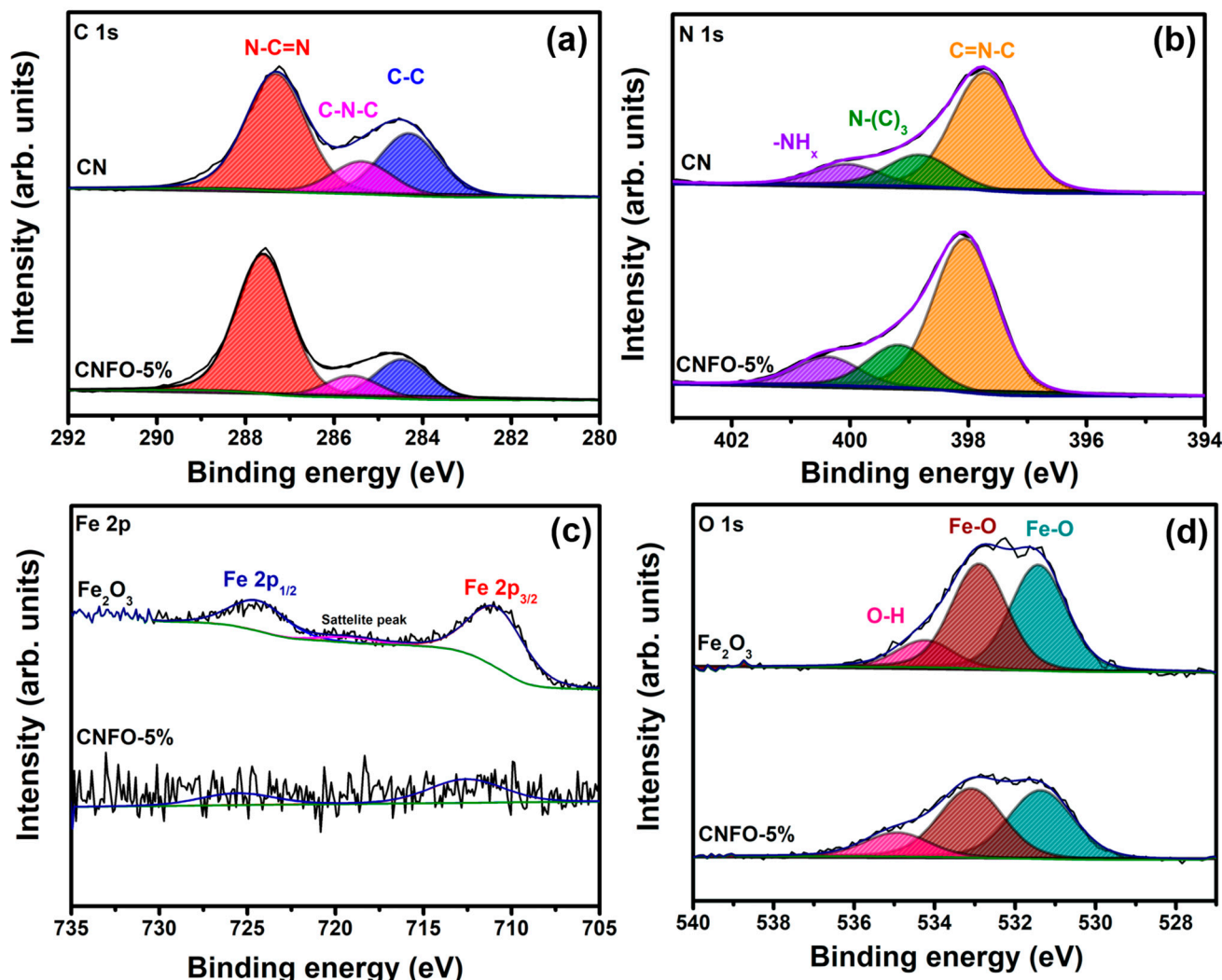


**Figure 6.** (a–d) Deconvoluted high-resolution XPS spectra for each element present in CN, FO, and CNFO-5% composite.

In Figure 6d, oxygen metal bonds of Fe-O are found at 531.3 and 532.9 eV. The oxygen species adsorbed to the surface O-H produce the peak at 534.5 eV [38]. Additionally, noticeable changes occurring in B.E. of each element after the formation of CNFO-5% composite confirm that CNFO heterojunction was successfully built [39]. The XPS valence band spectra were also used to calculate the valence band potentials. In Figure S2b, computed valence band positions for FO, CN, and CNFO-5% are 2.05, 1.55, and 1.65 eV, respectively.

The performance of synthesized photocatalysts were evaluated toward the degradation of 10 ppm OFX in the presence of Xe lamp (300 W,  $\lambda > 420$  nm). No photolysis of OFX occurred under visible light irradiation in the absence of a photocatalyst, indicating that OFX is quite a stable pollutant. Figure 7a depicts the photocatalytic degradation of OFX by various as-synthesized photocatalysts. Photocatalytic activity of pristine FO to photodegrade OFX remained poor even after prolonged light irradiation, perhaps as a result of a rapid charge-carrier recombination. The same reason restricted CN performance. CNFO-5% composite showed exceptional performance for OFX degradation within 30 min of light irradiation. However, when the FO content was further increased the activity was inhibited

due to the agglomeration of the catalyst. Pseudo-first-order reaction kinetics are depicted by linear graphs of  $-\ln(C/C_0)$  vs. the irradiation time for the photocatalytic degradation of OFX in Figure 7b. The initial rate constant of the CNFO-5% is 7.5 times faster than that of pure CN. The calculated initial rate constant for CN, CNFO-1%, CNFO-5%, and CNFO-10% are 0.0169, 0.0264, 0.1271, and 0.1194  $\text{min}^{-1}$ . The results of the photodegradation of OFX by various photocatalysts are tabulated in Table 1.

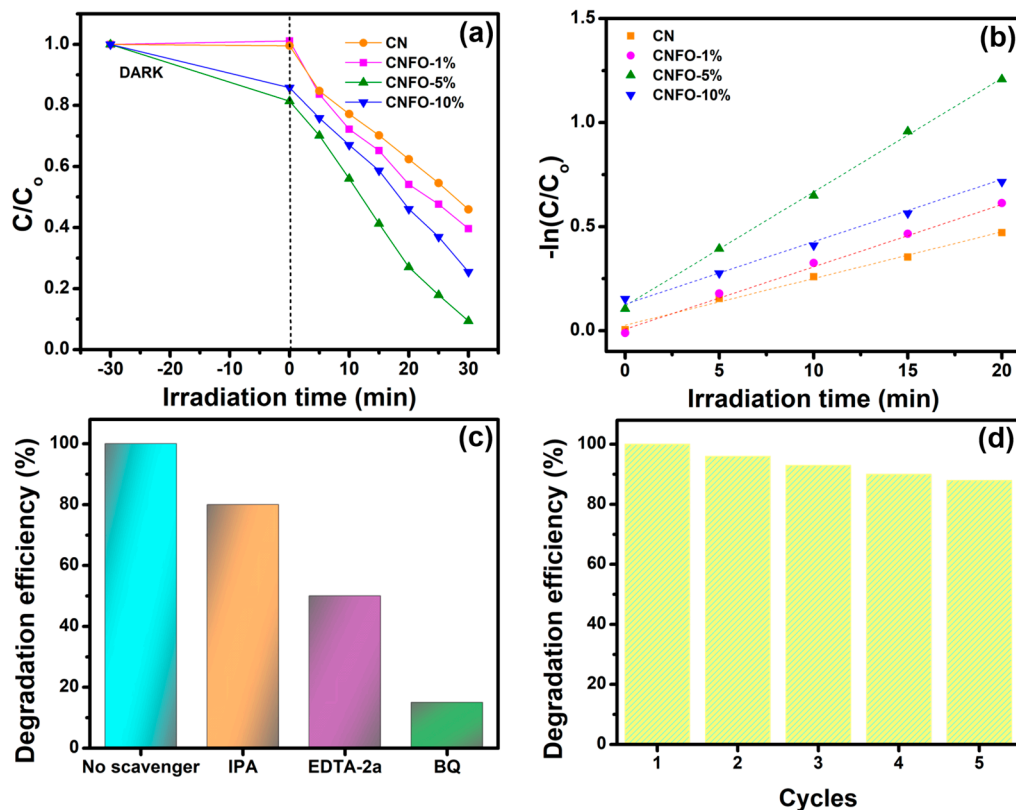


**Figure 7.** (a) Photodegradation of 10 ppm OFX, (b) their corresponding pseudo-first-order reaction kinetics, (c) performance of the photocatalyst in the presence of various scavengers, and (d) recycle and reuse of the catalyst for five cycles.

**Table 1.** The calculated bandgap, surface area, OFX degradation efficiency, and reaction rate constants for the as-synthesized photocatalysts.

Catalyst	Bandgap (eV)	Surface Area ( $\text{m}^2\text{g}^{-1}$ )	OFX Degradation Efficiency (%)	Reaction Rate Constant ( $\text{min}^{-1}$ )
CN	2.67	37	44	0.0169
FO	1.68	10	-	-
CNFO-1%	2.49	43	60	0.0264
CNFO-5%	2.48	50	93	0.1271
CNFO-10%	2.46	57	75	0.1194

The photodegradation of ofloxacin by various  $\text{g-C}_3\text{N}_4$ -based heterojunctions is compared in Table 2. In the current study, the mixed-phase ( $\alpha/\gamma\text{-Fe}_2\text{O}_3$ )/ $\text{g-C}_3\text{N}_4$  composite demonstrated the best performance in terms of ofloxacin photodegradation. Consequently, this composite is beneficial for effective wastewater treatment.

**Table 2.** Studies comparing the photodegradation efficiency of as-synthesized  $\alpha/\gamma\text{-Fe}_2\text{O}_3/g\text{-C}_3\text{N}_4$  to that of other  $\text{g}\text{-C}_3\text{N}_4$ -based composite photocatalysts reported in the literature.

Catalyst	Light Source	Degradation Efficiency (%), Time (min)	Type of Heterojunction	Ref.
$\text{BiVO}_4/g\text{-C}_3\text{N}_4/\text{NiFe}_2\text{O}_4$	300 W Xe lamp ( $\lambda > 420 \text{ nm}$ )	93.8, 20	Dual Z-scheme	[40]
$\text{g}\text{-C}_3\text{N}_4/\text{NH}_2\text{-MIL88B(Fe)}$	300 W Xe lamp ( $\lambda > 420 \text{ nm}$ )	96.5, 150	Type-II	[41]
$\text{g}\text{-C}_3\text{N}_4/\text{Ag}_3\text{PO}_4$	500 W Xe lamp	71.9, 10	Z-scheme	[42]
$\text{MoO}_3/\text{Ag}/\text{C}_3\text{N}_4$	150 W Xe lamp	96, 100	Z-scheme	[43]
$\text{NaNbO}_3/g\text{-C}_3\text{N}_4$	300 W Xe lamp	99.5, 30	Type-II	[44]
$\text{MnWO}_4/g\text{-C}_3\text{N}_4$	150 mW/cm <sup>2</sup> W lamp	90.4, 70	Type-II	[45]
$\text{MoO}_3/g\text{-C}_3\text{N}_4$	350 W Xe lamp ( $\lambda > 420 \text{ nm}$ )	94.4, 120	Z-scheme	[46]
$\alpha/\gamma\text{-Fe}_2\text{O}_3/g\text{-C}_3\text{N}_4$	300 W Xe lamp ( $\lambda > 420 \text{ nm}$ )	93, 30	Z-scheme	Present work

Using the radical trapping studies, we were able to identify the most important active radicals that were involved during the photodegradation of OFX in the presence of CNFO-5% composite. Section 3.5 provides a comprehensive explanation of the scavengers as well as the experimental conditions that were applied to the process. Under typical conditions, the CNFO-5% composite might totally decompose OFX in under 30 min (without scavenger). The rate of OFX degradation, by contrast, was reduced to 49% after EDTA-2Na was added to the reaction mixture. When BQ was utilized as a scavenger, the efficiency of OFX degradation dropped precipitously, all the way down to 15%. Therefore, photocatalytic degradation of OFX involves the influence from both  $\text{h}^+$  and  $\bullet\text{O}_2^-$  radicals. In addition, the photocatalytic performance of CNFO-5% was evaluated for five consecutive cycles by recycling the catalyst, as shown in Figure 7d. This was performed in order to determine the stability of the results. The loss of the photocatalyst that occurs with each cycle of centrifugation might account for some of the efficiency that is reduced as a result. The XRD patterns of the catalyst before and after use are recorded and shown in Figure S3a to confirm that it is stable even after the repeated photocatalytic reaction. Figure S3b represents the Fe 2p XPS spectra of the CNFO-5% after photocatalytic reaction. Negligible changes were observed in the oxidation state of the Fe, confirming its photostability.

Determining how charges are separated and transferred at the interface of the CNFO-5% composite is crucial. Only pure CN and the optimal composite CNFO-5% have been analyzed for photoluminescence (PL) and photoelectrochemical characterizations. As shown in Figure 8a, band-to-band PL can be attributed to the broad emission peak in pure CN at 460 nm that occurs from charge-carrier recombination [47]. In addition, the formation of the CNFO heterojunction with a strong contact may result in significant PL quenching in the composite, which would imply less carrier recombination and improved charge separation [48]. Figure 8b represents the Nyquist plots for the synthesized photocatalysts. The electrolyte and electrical resistance of the photoelectrodes account for the higher frequency area/semicircle region, which indicates charge-transfer resistance and space-charge diffusion in the electrode/electrolyte system [49]. The CNFO-5% composite had the lowest charge-transfer resistance compared to pure CN, as shown by the narrower arc.

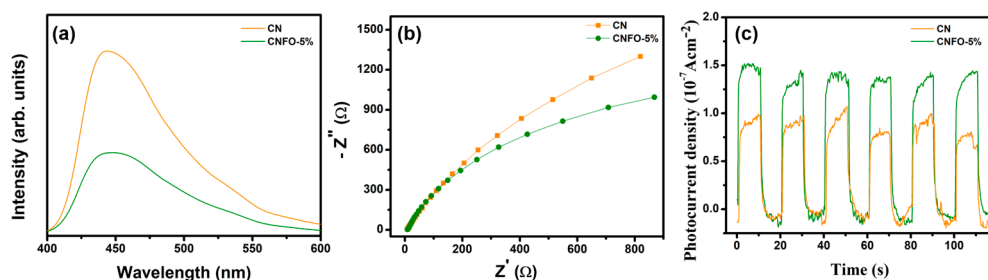
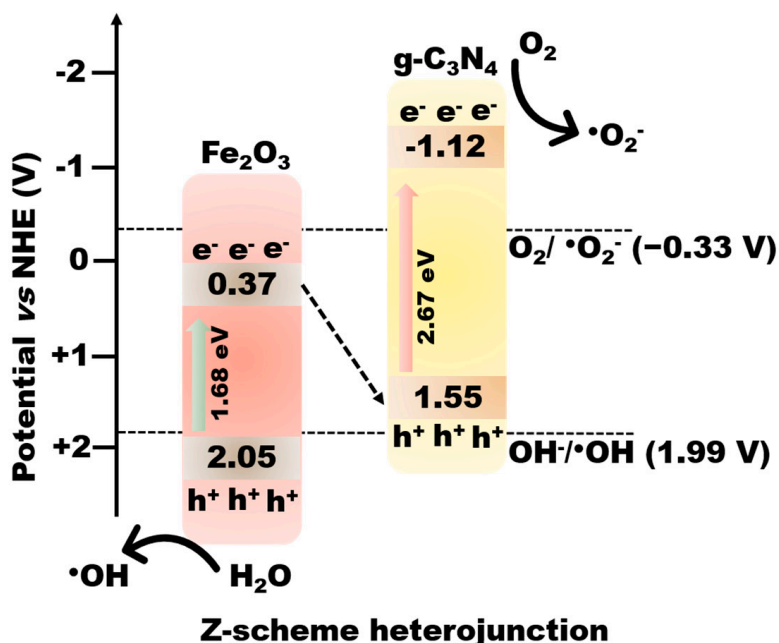


**Figure 8.** (a) Photoluminescence spectra, (b) Nyquist plot, and (c) photocurrent density measurements of as-synthesized CN and CNFO-5% composite.

Figure 8c demonstrates that the CNFO-5% composite exhibited the maximum photocurrent intensity, indicating the most effective separation of photogenerated holes and electrons across their heterojunction. The results obtained agree with those from the photocatalysis data and PL experiments.

The conduction band edges ( $E_{CB}$ ) of CN, FO, and CNFO-5% composites was determined using the equation  $E_{CB} = E_{VB} - E_g$ , allowing for a more in-depth assessment of their band edge positions. The bandgap and valence band edges are determined from UV-DRS and XPS studies as discussed in the previous section. Based on the calculated band edges, Scheme 1 shows the band alignment of the CNFO composite and explains the detailed Z-scheme structure mechanism.



**Scheme 1.** Proposed mechanism for charge-carrier separation and transfer at CN and FO heterojunction.

The well-matched band structure between CN and FO allows for the formation of an internal electrical field in the direction from CN to FO. When exposed to visible light, excited electrons transfer from the  $E_{CB}$  of CN to that of FO, and photoinduced holes would typically move in the other direction. Thermodynamically, no •O<sub>2</sub><sup>-</sup> radicals can be formed over CB of FO since its  $E_{CB}$  (0.37 V) is lower than standard potential of O<sub>2</sub>/•O<sub>2</sub><sup>-</sup> (-0.33 V). Additionally, the formation of •OH is prohibited by the  $E_{VB}$  of CN (1.55 eV), which is more negative than H<sub>2</sub>O/•OH (1.99 V). Therefore, it is suggested that a photocatalytic system be built according to the Z-scheme as depicted in Scheme 1. In a Z-scheme mechanism, the strong reducing ability of electrons in the  $E_{CB}$  of CN and the strong oxidizing ability of holes in the  $E_{VB}$  of FO are maintained as the excited conduction band electrons in FO migrate to the interface to pair with the photoinduced valence band holes of CN. Hence,

the electrons on the  $E_{CB}$  of CN and holes on the  $E_{VB}$  of FO undergo reduction and oxidation to generate highly reactive radical species, which further degrade the OFX molecules.

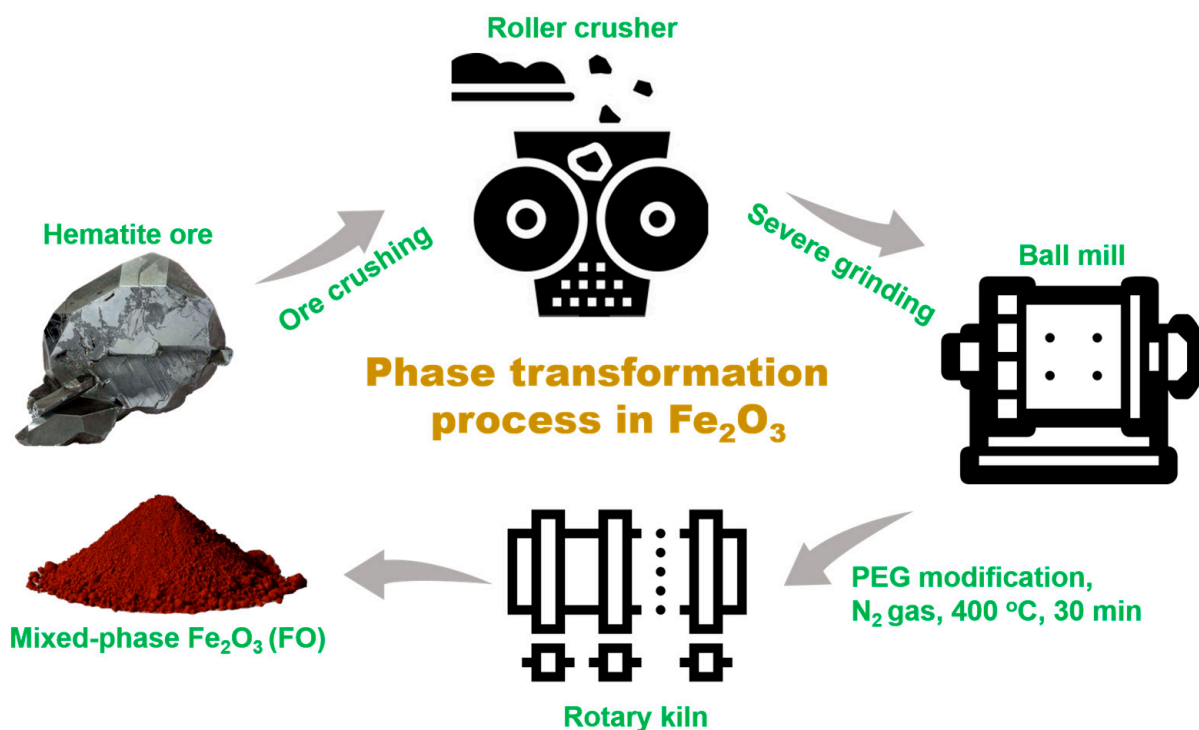
### 3. Materials and Methods

#### 3.1. Chemicals

Hematite ore ( $\alpha\text{-Fe}_2\text{O}_3$ , 99%) hand-picked specimen was received from Minas Gerais area, Brazil. Polyethylene glycol (PEG, 98%), urea ( $\text{CH}_4\text{N}_2\text{O}$ , 99%), para-benzoquinone (BQ) ( $\text{C}_6\text{H}_4\text{O}_2$ , 98%), ethylenediaminetetraacetic acid disodium (EDTA-2Na) ( $\text{C}_{10}\text{H}_{14}\text{N}_2\text{Na}_2\text{O}_8$ , 99%), and isopropyl alcohol (IPA) ( $\text{C}_3\text{H}_8\text{O}$ , 99.7%) were received from Wako Chemicals, Osaka, Japan. Deionized water (DI  $\text{H}_2\text{O}$ ) was utilized throughout the experiment.

#### 3.2. Partial Phase Transformation of Natural Hematite

A specimen of high-grade (99%) hematite that had been hand-picked in the Minas Gerais area of Brazil was received. Following the previously reported literature [38] with some modifications, mixed-phase  $\text{Fe}_2\text{O}_3$  was synthesized. Crushing, followed by grinding in a ball mill, and screening resulted in a –75 micron-size fraction being obtained from the material. This sample, which weighed 1 g, was completely combined with 0.05 g of powder that contained polyethylene glycol (PEG). The combination was subjected to 400 °C heat treatment for time interval of 30 min in an inert environment ( $\text{N}_2$ ) inside of a rotary kiln manufactured by Motoyama (MS-4188). The mixed-phase  $\text{Fe}_2\text{O}_3$  that was obtained will be denoted as FO from this point forward. Diagrammatically, the complete experimental technique is shown in Scheme 2.



**Scheme 2.** Phase transformation process in hematite ore.

#### 3.3. Synthesis of CNFO-X% Composites and Pristine $\text{g-C}_3\text{N}_4$

To obtain CNFO-X% composites, 10 g of urea was mixed with X = 1, 5, and 10 weight % of as-synthesized FO and calcined in furnace at 550 °C, 2 h,  $10^{\circ}\text{Cmin}^{-1}$ . The obtained products are referred as CNFO-1%, CNFO-5%, and CNFO-10%, respectively. Pure  $\text{g-C}_3\text{N}_4$ , which will be referred to as CN from here on, was synthesized in identical experimental conditions utilizing urea as the starting source.

### 3.4. Characterization

A Rigaku Ultima IV diffractometer was utilized in order to investigate the X-ray diffraction (XRD) patterns of the synthesized photocatalysts. At the Kyushu Synchrotron Light Research Centre, also known as SAGA-LS, in Tosa, Japan, all the as-synthesized catalysts were subjected to measurements using the transmission mode of BL15 Fe K-edge XANES spectroscopy. When the samples had been diluted with boron nitride, Kapton tape was used to secure them for further examination. We were able to scan the photon energy from 8.9 keV all the way up to 9.2 keV by using a silicon double crystal monochromator. For the purpose of analyzing the morphology of the samples that were produced, a Keyence VE-9800 scanning electron microscope was utilized. The presence of each element in the synthesized photocatalyst, elemental mapping was conducted, which showed the existence of C, N, Fe, and O in the CN-FO composite. A Shimadzu UV-2450 spectrophotometer was utilized in order to investigate the optical characteristics. Barium sulphate powder is used as the reference while measuring their optical properties. The chemical states of the photocatalysts and their valence band positions were identified by using an ESCA 5800, ULVAC-PHI X-ray photoelectron spectroscopy. Calibration of the orbitals was accomplished by using the binding energies of [C 1 s], which were set at  $E = 284.6$  eV. For the purpose of determining the Brunauer–Emmett–Teller surface area of the samples, a Belsorp-mini II device was utilized. In order to acquire the energy-resolved distribution of the electron trap (ERDT) patterns of the synthesized samples, the reversed double-beam photoacoustic spectroscopy (RDB-PAS) technique was utilized. This technique involved the use of an amplifier in order to enhance the photoacoustic signals.

### 3.5. Photocatalytic Degradation of Ofloxacin

The photocatalytic activity of the as-prepared photocatalysts was tested by observing the rate at which ofloxacin (OFX) was degraded in the presence of visible light. At the beginning,  $1\text{ g L}^{-1}$  of the catalyst was dispersed in 50 mL of 10 ppm OFX solution. In order to achieve an equilibrium between adsorption and desorption, the reaction slurry was agitated in the dark for a period of thirty minutes. After this, the mixture that was stirred in the dark was exposed to visible light (Xe lamp, 300 W,  $>420$  nm). During the photocatalytic process, aliquots of 5 mL were obtained at regular intervals of time and filtered through polytetrafluoroethylene filters with a pore size of  $0.45\text{ }\mu\text{m}$ . Using a UV-Vis spectrophotometer, an evaluation of the reduction in the concentration of OFX is carried out by measuring the compound's absorption (Implen nanophotometer). The approach that was stated in the earlier scientific literature was followed in order to ascertain the photocatalysts levels of activity. The hydroxyl radicals ( $\bullet\text{OH}$ ), superoxide anion radicals ( $\bullet\text{O}_2^-$ ), and holes were scavenged by chemicals, such as isopropanol (IPA), para-benzoquinone (BQ), and ethylenediaminetetraacetic acid disodium (EDTA-2Na). Typically, 5 mM of the suitable scavenger is added to the 10 ppm OFX solution containing  $1\text{ g L}^{-1}$  of the catalyst, and the photocatalytic reaction is carried out as discussed above. The performance of the synthesized catalysts for the photodegradation 10 ppm OFX in the presence of scavenger confirmed the involvement of active radicals in the degradation process.

## 4. Conclusions

This study describes the use of abundantly available natural hematite ore ( $\text{Fe}_2\text{O}_3$ ) for the degradation of pharmaceutical wastewater pollutants. We demonstrate herein that a simple heat treatment process can successfully transform  $\text{Fe}_2\text{O}_3$  into its heterophase, which is characterized by the presence of alpha and gamma phases ( $\alpha/\gamma\text{-Fe}_2\text{O}_3$ ). In addition,  $\text{g-C}_3\text{N}_4\text{-Fe}_2\text{O}_3$  (CNFO) composites were produced through an in-situ reaction between as-prepared  $\alpha/\gamma\text{-Fe}_2\text{O}_3$  and urea, the precursor for  $\text{g-C}_3\text{N}_4$ . The heterojunction formed by the combination of CN and FO increased the visible light absorption capacity of pristine CN. Moreover, the FO particles supported the growth of CN nanosheets on its surface, preventing its agglomeration and increasing the surface area. Furthermore, the introduction of FO generates some surface defect in CN, which results in the generation of new electron

trap states on the surface of CN as evidenced from ERDT patterns. The formation of new electron trap states with energies was beneficial as these states trapped photoinduced charges and hindered their recombination rate. When compared to pure CN, the CNFO-5% composite demonstrated 7.5 times more photocatalytic activity in degrading ofloxacin under visible light conditions. The initial rate constant value for the photocatalytic degradation of OFX by CNFO-5% was  $0.1271 \text{ min}^{-1}$ . The catalyst was quite stable, even after five repeated cycles of photodegradation. The photoluminescence analysis and electrochemical measurements confirmed the efficient separation and transfer of the photogenerated charges across their interface. The investigations on different scavengers demonstrated that superoxide anion radicals and holes played a significant role in the degradation of ofloxacin. The proposed charge-transfer pathway in CNFO composite relied on the band edge positions determined by XPS analysis. In addition, the CNFO composite formed a Z-scheme heterojunction, which improved charge-carrier separation at the interface and led to an overall improvement in photocatalytic performance. This heterophase of  $\text{Fe}_2\text{O}_3$  can be coupled with other wide bandgap semiconductors to form heterojunctions, and their performance can be evaluated for both environmental remediation and the production of clean energy.

**Supplementary Materials:** The following supporting information can be downloaded at: <https://www.mdpi.com/article/10.3390/catal13050792/s1>, Figure S1: UV-Visible absorption spectra of  $\alpha\text{-Fe}_2\text{O}_3$  and mixed-phase  $\text{Fe}_2\text{O}_3$ ; Figure S2: (a) XPS survey spectrum and (b) calculated band edge positions from XPS spectra; Figure S3: (a) XRD and (b) XPS spectra of the CNFO-5% catalyst after the photodegradation experiments.

**Author Contributions:** S.S.: Conceptualization, methodology, validation, formal analysis, investigation, data curation, writing—original draft preparation, writing—review and editing, visualization, M.M.F.: methodology, investigation, data curation, C.C., K.S. (Karthikeyan Sekar), B.R.: formal analysis, K.S. (Keiko Sasaki): supervision, review, and editing. All authors have read and agreed to the published version of the manuscript.

**Funding:** The authors are grateful to the Japan Society for the Promotion of Science (JSPS) for funding the research grants (JP21F21342, JP22H00266) to KS and a postdoctoral fellowship for foreign researchers (JP 21P21342) to SS.

**Data Availability Statement:** Not applicable.

**Acknowledgments:** The authors would like to express their gratitude to the Kyushu University Nanotech Center for giving access to XPS measurements and BET analysis.

**Conflicts of Interest:** The authors declare no conflict of interest.

## References

1. de Souza, H.O.; dos Costa, R.S.; Quadra, G.R.; dos Fernandez, M.A.S. Pharmaceutical Pollution and Sustainable Development Goals: Going the Right Way? *Sustain. Chem. Pharm.* **2021**, *21*, 100428. [[CrossRef](#)]
2. Wilkinson, J.L.; Boxall, A.B.A.; Kolpin, D.W.; Leung, K.M.Y.; Lai, R.W.S.; Galbán-Malagón, C.; Adell, A.D.; Mondon, J.; Metian, M.; Marchant, R.A.; et al. Pharmaceutical Pollution of the World's Rivers. *Proc. Natl. Acad. Sci. USA* **2022**, *119*, e2113947119. [[CrossRef](#)] [[PubMed](#)]
3. Ta, Q.T.H.; Cho, E.; Sreedhar, A.; Noh, J.-S. Mixed-Dimensional, Three-Level Hierarchical Nanostructures of Silver and Zinc Oxide for Fast Photocatalytic Degradation of Multiple Dyes. *J. Catal.* **2019**, *371*, 1–9. [[CrossRef](#)]
4. Peres, M.S.; Maniero, M.G.; Guimarães, J.R. Photocatalytic Degradation of Ofloxacin and Evaluation of the Residual Antimicrobial Activity. *Photochem. Photobiol. Sci.* **2015**, *14*, 556–562. [[CrossRef](#)] [[PubMed](#)]
5. Gao, P.; Tian, X.; Nie, Y.; Yang, C.; Zhou, Z.; Wang, Y. Promoted Peroxymonosulfate Activation into Singlet Oxygen over Perovskite for Ofloxacin Degradation by Controlling the Oxygen Defect Concentration. *Chem. Eng. J.* **2019**, *359*, 828–839. [[CrossRef](#)]
6. Mahlaule-Glory, L.M.; Mathobela, S.; Hintsho-Mbita, N.C. Biosynthesized Bimetallic ( $\text{ZnOSnO}_2$ ) Nanoparticles for Photocatalytic Degradation of Organic Dyes and Pharmaceutical Pollutants. *Catalysts* **2022**, *12*, 334. [[CrossRef](#)]
7. Fedorov, K.; Dinesh, K.; Sun, X.; Soltani, R.D.; Wang, Z.; Sonawane, S.; Boczkaj, G. Synergistic Effects of Hybrid Advanced Oxidation Processes (AOPs) Based on Hydrodynamic Cavitation Phenomenon—A Review. *Chem. Eng. J.* **2022**, *432*, 134191. [[CrossRef](#)]

8. Ge, J.; Zhang, Y.; Heo, Y.-J.; Park, S.-J. Advanced Design and Synthesis of Composite Photocatalysts for the Remediation of Wastewater: A Review. *Catalysts* **2019**, *9*, 122. [[CrossRef](#)]
9. Zhou, P.; Navid, I.A.; Ma, Y.; Xiao, Y.; Wang, P.; Ye, Z.; Zhou, B.; Sun, K.; Mi, Z. Solar-to-Hydrogen Efficiency of More than 9% in Photocatalytic Water Splitting. *Nature* **2023**, *613*, 66–70. [[CrossRef](#)]
10. Liu, C.; Zhang, Q.; Zou, Z. Recent Advances in Designing  $ZnIn_2S_4$ -Based Heterostructured Photocatalysts for Hydrogen Evolution. *J. Mater. Sci. Technol.* **2023**, *139*, 167–188. [[CrossRef](#)]
11. Antonopoulou, M.; Papadaki, M.; Rapti, I.; Konstantinou, I. Photocatalytic Degradation of Pharmaceutical Amisulpride Using  $G-C_3N_4$  Catalyst and UV-A Irradiation. *Catalysts* **2023**, *13*, 226. [[CrossRef](#)]
12. Thi, L.N.; Phan, T.T.T.; Ngoc, T.N.; Viswanath, N.S.M.; Le, H.T.T.; Tran Thi, L.; Tien-Trung, N.; Nguyen, L.T.; Nghiem, D.N.; Tran Huu, H.; et al. Prussian Blue Decorated  $G-C_3N_4$ —From Novel Synthesis to Insight Study on Charge Transfer Strategy for Improving Visible-Light Driven Photo-Fenton Catalytic Activity. *J. Alloys Compd.* **2022**, *916*, 165331. [[CrossRef](#)]
13. Wen, J.; Xie, J.; Chen, X.; Li, X. A Review on  $G-C_3N_4$ -Based Photocatalysts. *Appl. Surf. Sci.* **2017**, *391*, 72–123. [[CrossRef](#)]
14. Wang, H.; Zhang, L.; Chen, Z.; Hu, J.; Li, S.; Wang, Z.; Liu, J.; Wang, X. Semiconductor Heterojunction Photocatalysts: Design, Construction, and Photocatalytic Performances. *Chem. Soc. Rev.* **2014**, *43*, 5234–5244. [[CrossRef](#)]
15. Konstas, P.-S.; Konstantinou, I.; Petrakis, D.; Albanis, T. Synthesis, Characterization of  $g-C_3N_4/SrTiO_3$  Heterojunctions and Photocatalytic Activity for Organic Pollutants Degradation. *Catalysts* **2018**, *8*, 554. [[CrossRef](#)]
16. Hanif, M.A.; Akter, J.; Kim, Y.S.; Kim, H.G.; Hahn, J.R.; Kwac, L.K. Highly Efficient and Sustainable  $ZnO/CuO/g-C_3N_4$  Photocatalyst for Wastewater Treatment under Visible Light through Heterojunction Development. *Catalysts* **2022**, *12*, 151. [[CrossRef](#)]
17. Wang, Z.; Lin, Z.; Shen, S.; Zhong, W.; Cao, S. Advances in Designing Heterojunction Photocatalytic Materials. *Chin. J. Catal.* **2021**, *42*, 710–730. [[CrossRef](#)]
18. Ong, W.-J.; Tan, L.-L.; Ng, Y.H.; Yong, S.-T.; Chai, S.-P. Graphitic Carbon Nitride ( $g-C_3N_4$ )-Based Photocatalysts for Artificial Photosynthesis and Environmental Remediation: Are We a Step Closer To Achieving Sustainability? *Chem. Rev.* **2016**, *116*, 7159–7329. [[CrossRef](#)]
19. Li, Y.; Xia, Z.; Yang, Q.; Wang, L.; Xing, Y. Review on  $G-C_3N_4$ -Based S-Scheme Heterojunction Photocatalysts. *J. Mater. Sci. Technol.* **2022**, *125*, 128–144. [[CrossRef](#)]
20. Ziaur Rahman, M.; Golam Kibria, M.; Buddie Mullins, C. Metal-Free Photocatalysts for Hydrogen Evolution. *Chem. Soc. Rev.* **2020**, *49*, 1887–1931. [[CrossRef](#)]
21. Védrine, J.C. Heterogeneous Catalysis on Metal Oxides. *Catalysts* **2017**, *7*, 341. [[CrossRef](#)]
22. Wu, W.; Jiang, C.; Roy, V.A. Recent Progress in Magnetic Iron Oxide–Semiconductor Composite Nanomaterials as Promising Photocatalysts. *Nanoscale* **2015**, *7*, 38–58. [[CrossRef](#)]
23. Singh, P.; Sharma, K.; Hasija, V.; Sharma, V.; Sharma, S.; Raizada, P.; Singh, M.; Saini, A.K.; Hosseini-Bandegharaei, A.; Thakur, V.K. Systematic Review on Applicability of Magnetic Iron Oxides–Integrated Photocatalysts for Degradation of Organic Pollutants in Water. *Mater. Today Chem.* **2019**, *14*, 100186. [[CrossRef](#)]
24. Mishra, M.; Chun, D.-M.  $\alpha$ - $Fe_2O_3$  as a Photocatalytic Material: A Review. *Appl. Catal. A Gen.* **2015**, *498*, 126–141. [[CrossRef](#)]
25. Thakur, D.; Ta, Q.T.H.; Noh, J.-S. Photon-Induced Superior Antibacterial Activity of Palladium-Decorated, Magnetically Separable  $Fe_3O_4/Pd/Mg-C_3N_4$  Nanocomposites. *Molecules* **2019**, *24*, 3888. [[CrossRef](#)]
26. Li, X.; Qiu, Y.; Zhu, Z.; Chen, T.; Zhang, H.; Yin, D. Construction of Magnetically Separable Dual Z-Scheme  $g-C_3N_4/\alpha$ - $Fe_2O_3/Bi_3TaO_7$  Photocatalyst for Effective Degradation of Ciprofloxacin under Visible Light. *Chem. Eng. J.* **2022**, *440*, 135840. [[CrossRef](#)]
27. Lin, Y.-F.; Chang, C.-Y. Design of Composite Maghemite/Hematite/Carbon Aerogel Nanostructures with High Performance for Organic Dye Removal. *Sep. Purif. Technol.* **2015**, *149*, 74–81. [[CrossRef](#)]
28. Baig, U.; Gondal, M.A.; Dastageer, M.A.; Sajid, M. Maghemite Nanoparticles Decorated Semiconducting Graphitic Carbon Nitride Hetero-Structured Nanocomposite: Facile Synthesis, Characterizations and Its Visible Light Active Photocatalytic System for Removal of Hazardous Organic Pollutants from Aqueous Solutions. *Colloids Surf. A Physicochem. Eng. Asp.* **2022**, *641*, 128427. [[CrossRef](#)]
29. Ghasemifard, M.; Heidari, G.; Ghamsari, M.; Fathi, E.; Izzi, M. Synthesis of Porous Network-Like  $\alpha$ - $Fe_2O_3$  and  $\alpha/\gamma$ - $Fe_2O_3$  Nanoparticles and Investigation of Their Photocatalytic Properties. *Nanotechnol. Russ.* **2019**, *14*, 353–361. [[CrossRef](#)]
30. Li, F.; Liu, Y.; Sun, Z.; Zhao, Y.; Liu, R.; Chen, L.; Zhao, D. Photocatalytic Oxidative Desulfurization of Dibenzothiophene under Simulated Sunlight Irradiation with Mixed-Phase  $Fe_2O_3$  Prepared by Solution Combustion. *Catal. Sci. Technol.* **2012**, *2*, 1455–1462. [[CrossRef](#)]
31. Sridharan, K.; Kuriakose, T.; Philip, R.; Park, T.J. Transition Metal (Fe, Co and Ni) Oxide Nanoparticles Grafted Graphitic Carbon Nitrides as Efficient Optical Limiters and Recyclable Photocatalysts. *Appl. Surf. Sci.* **2014**, *308*, 139–147. [[CrossRef](#)]
32. Shenoy, S.; Chuaiacham, C.; Okumura, T.; Sekar, K.; Sasaki, K. Simple Tactic Polycondensation Synthesis of Z-Scheme Quasi-Polymeric  $g-C_3N_4/CaFe_2O_4$  Composite for Enhanced Photocatalytic Water Depollution via p-n Heterojunction. *Chem. Eng. J.* **2023**, *453*, 139758. [[CrossRef](#)]
33. Deraz, N.M.; Alarifi, A. Novel Processing and Magnetic Properties of Hematite/Maghemic Nano-Particles. *Ceram. Int.* **2012**, *38*, 4049–4055. [[CrossRef](#)]

34. Shenoy, S.; Tarafder, K.; Sridharan, K. Graphitic C<sub>3</sub>N<sub>4</sub>/CdS Composite Photocatalyst: Synthesis, Characterization and Photodegradation of Methylene Blue under Visible Light. *Phys. B Condens. Matter* **2020**, *595*, 412367. [CrossRef]
35. Shenoy, S.; Jang, E.; Park, T.J.; Gopinath, C.S.; Sridharan, K. Cadmium Sulfide Nanostructures: Influence of Morphology on the Photocatalytic Degradation of Erioglaucine and Hydrogen Generation. *Appl. Surf. Sci.* **2019**, *483*, 696–705. [CrossRef]
36. Chuaicham, C.; Noguchi, Y.; Shenoy, S.; Shu, K.; Trakulmututa, J.; Srikaow, A.; Sekar, K.; Sasaki, K. Simultaneous Photocatalytic Sugar Conversion and Hydrogen Production Using Pd Nanoparticles Decorated on Iron-Doped Hydroxyapatite. *Catalysts* **2023**, *13*, 675. [CrossRef]
37. Xu, Q.; Zhu, B.; Jiang, C.; Cheng, B.; Yu, J. Constructing 2D/2D Fe<sub>2</sub>O<sub>3</sub>/g-C<sub>3</sub>N<sub>4</sub> Direct Z-Scheme Photocatalysts with Enhanced H<sub>2</sub> Generation Performance. *Sol. RRL* **2018**, *2*, 1800006. [CrossRef]
38. Sanad, M.M.S.; Farahat, M.M.; El-Hout, S.I.; El-Sheikh, S.M. Preparation and Characterization of Magnetic Photocatalyst from the Banded Iron Formation for Effective Photodegradation of Methylene Blue under UV and Visible Illumination. *J. Environ. Chem. Eng.* **2021**, *9*, 105127. [CrossRef]
39. Jiang, Z.; Wan, W.; Li, H.; Yuan, S.; Zhao, H.; Wong, P.K. A Hierarchical Z-Scheme  $\alpha$ -Fe<sub>2</sub>O<sub>3</sub>/g-C<sub>3</sub>N<sub>4</sub> Hybrid for Enhanced Photocatalytic CO<sub>2</sub> Reduction. *Adv. Mater.* **2018**, *30*, 1706108. [CrossRef] [PubMed]
40. Zhao, G.; Ding, J.; Zhou, F.; Chen, X.; Wei, L.; Gao, Q.; Wang, K.; Zhao, Q. Construction of a Visible-Light-Driven Magnetic Dual Z-Scheme BiVO<sub>4</sub>/g-C<sub>3</sub>N<sub>4</sub>/NiFe<sub>2</sub>O<sub>4</sub> Photocatalyst for Effective Removal of Ofloxacin: Mechanisms and Degradation Pathway. *Chem. Eng. J.* **2021**, *405*, 126704. [CrossRef]
41. Su, Q.; Li, J.; Yuan, H.; Wang, B.; Wang, Y.; Li, Y.; Xing, Y. Visible-Light-Driven Photocatalytic Degradation of Ofloxacin by g-C<sub>3</sub>N<sub>4</sub>/NH<sub>2</sub>-MIL-88B(Fe) Heterostructure: Mechanisms, DFT Calculation, Degradation Pathway and Toxicity Evolution. *Chem. Eng. J.* **2022**, *427*, 131594. [CrossRef]
42. Chen, R.; Ding, S.; Fu, N.; Ren, X. Preparation of a G-C<sub>3</sub>N<sub>4</sub>/Ag<sub>3</sub>PO<sub>4</sub> Composite Z-Type Photocatalyst and Photocatalytic Degradation of Ofloxacin: Degradation Performance, Reaction Mechanism, Degradation Pathway and Toxicity Evaluation. *J. Environ. Chem. Eng.* **2023**, *11*, 109440. [CrossRef]
43. Adhikari, S.; Lee, H.H.; Kim, D.-H. Efficient Visible-Light Induced Electron-Transfer in z-Scheme MoO<sub>3</sub>/Ag/C<sub>3</sub>N<sub>4</sub> for Excellent Photocatalytic Removal of Antibiotics of Both Ofloxacin and Tetracycline. *Chem. Eng. J.* **2020**, *391*, 123504. [CrossRef]
44. Zhang, D.; Qi, J.; Ji, H.; Li, S.; Chen, L.; Huang, T.; Xu, C.; Chen, X.; Liu, W. Photocatalytic Degradation of Ofloxacin by Perovskite-Type NaNbO<sub>3</sub> Nanorods Modified g-C<sub>3</sub>N<sub>4</sub> Heterojunction under Simulated Solar Light: Theoretical Calculation, Ofloxacin Degradation Pathways and Toxicity Evolution. *Chem. Eng. J.* **2020**, *400*, 125918. [CrossRef]
45. Saravanan Kumar, K.; Mamba, G.; Muthuraj, V. 1D/2D MnWO<sub>4</sub> Nanorods Anchored on g-C<sub>3</sub>N<sub>4</sub> Nanosheets for Enhanced Photocatalytic Degradation Ofloxacin under Visible Light Irradiation. *Colloids Surf. A Physicochem. Eng. Asp.* **2019**, *581*, 123845. [CrossRef]
46. Chen, D.; Xie, Z.; Zeng, Y.; Lv, W.; Zhang, Q.; Wang, F.; Liu, G.; Liu, H. Accelerated Photocatalytic Degradation of Quinolone Antibiotics over Z-Scheme MoO<sub>3</sub>/g-C<sub>3</sub>N<sub>4</sub> Heterostructure by Peroxydisulfate under Visible Light Irradiation: Mechanism; Kinetic; and Products. *J. Taiwan Inst. Chem. Eng.* **2019**, *104*, 250–259. [CrossRef]
47. Dao, D.Q.; Nguyen, T.K.A.; Pham, T.-T.; Shin, E.W. Synergistic Effect on Photocatalytic Activity of Co-Doped NiTiO<sub>3</sub>/g-C<sub>3</sub>N<sub>4</sub> Composites under Visible Light Irradiation. *Catalysts* **2020**, *10*, 1332. [CrossRef]
48. Lee, G.-J.; Lee, X.-Y.; Lyu, C.; Liu, N.; Andandan, S.; Wu, J.J. Sonochemical Synthesis of Copper-Doped BiVO<sub>4</sub>/g-C<sub>3</sub>N<sub>4</sub> Nanocomposite Materials for Photocatalytic Degradation of Bisphenol A under Simulated Sunlight Irradiation. *Nanomaterials* **2020**, *10*, 498. [CrossRef]
49. Zhao, Y.; Shi, H.; Yang, D.; Fan, J.; Hu, X.; Liu, E. Fabrication of a Sb<sub>2</sub>MoO<sub>6</sub>/g-C<sub>3</sub>N<sub>4</sub> Photocatalyst for Enhanced RhB Degradation and H<sub>2</sub> Generation. *J. Phys. Chem. C* **2020**, *124*, 13771–13778. [CrossRef]

**Disclaimer/Publisher’s Note:** The statements, opinions and data contained in all publications are solely those of the individual author(s) and contributor(s) and not of MDPI and/or the editor(s). MDPI and/or the editor(s) disclaim responsibility for any injury to people or property resulting from any ideas, methods, instructions or products referred to in the content.